



OPEN

## Revealing the dynamics of ultrarelativistic non-equilibrium many-electron systems with phase space tomography

Stefan Funkner<sup>1✉</sup>, Gudrun Niehues<sup>1</sup>, Michael J. Nasse<sup>1</sup>, Erik Bründermann<sup>1</sup>, Michele Caselle<sup>1</sup>, Benjamin Kehrer<sup>1</sup>, Lorenzo Rota<sup>1,3</sup>, Patrik Schönfeldt<sup>1,4</sup>, Marcel Schuh<sup>1</sup>, Bernd Steffen<sup>2</sup>, Johannes L. Steinmann<sup>1</sup>, Marc Weber<sup>1</sup> & Anke-Susanne Müller<sup>1</sup>

The description of physical processes with many-particle systems is a key approach to the modeling of numerous physical systems. For example in storage rings, where ultrarelativistic particles are agglomerated in dense bunches, the modeling and measurement of their phase-space distribution is of paramount importance: at any time the phase-space distribution not only determines the complete space-time evolution but also provides fundamental performance characteristics for storage ring operation. Here, we demonstrate a non-destructive tomographic imaging technique for the 2D longitudinal phase-space distribution of ultrarelativistic electron bunches. For this purpose, we utilize a unique setup, which streams turn-by-turn near-field measurements of bunch profiles at MHz repetition rates. To demonstrate the feasibility of our method, we induce a non-equilibrium state and show that the phase-space distribution microstructuring as well as the phase-space distribution dynamics can be observed in great detail. Our approach offers a pathway to control ultrashort bunches and supports, as one example, the development of compact accelerators with low energy footprints.

The modeling of systems composed of a large number of interacting particles are of utmost importance in physics<sup>1</sup> with applications ranging from molecular dynamics simulations<sup>2</sup>, the description of traffic dynamics<sup>3</sup> to the treatment of quantized many-particle systems<sup>4</sup>.

One model for such a system is the many-electron system. In applications, it can be affected by relativistic effects, quantized emission of photons and coherence, if it is spatially compressed. For example, relativistic free electrons are utilized in particle accelerators for high-energy physics experiments and the generation of synchrotron radiation. In the latter case, the fact that accelerated ultrarelativistic electrons produce broadband emission from the microwave to the hard x-ray range is harnessed in evermore advanced synchrotron light sources throughout the world for widespread applications in science, industry and medicine.

For such applications, accelerator-based light sources need to provide stable emission. This is achieved by storage rings, where the particles circulate in pulsed structures consisting of electron bunches. If sufficiently compressed longitudinally, these bunches emit coherent synchrotron radiation (CSR) at wavelengths corresponding to the Fourier transform of their longitudinal density profile<sup>5–7</sup>. Compared to incoherent radiation, CSR can be several orders of magnitude higher in intensity, which makes it particularly interesting for user applications. Hence, to provide an increasing brilliance at frequencies in the THz range and above<sup>8</sup> to accelerator users, scientists aim to increase the electron density by compressing the bunch as short as possible.

However, there is a trade-off to this optimization: above a certain density threshold the collective radiation field exerts significant forces on the particles leading to a buildup and self-amplification of substructures on the bunch profile. The formation, growth and subsequent dissipation or collapse of such substructures together with the associated dynamics is called microbunching instability (MBI). As a consequence, irregular bursts of CSR are emitted<sup>9,10</sup>, that can be even more intense than the CSR emission at short wavelengths during stable bunch formation at an electron density below the stability threshold<sup>11</sup>. The MBI is the main limiting factor for the generation of stable and intense CSR in storage rings run in short bunch mode.

<sup>1</sup>Karlsruhe Institute of Technology, 76344 Eggenstein-Leopoldshafen, Germany. <sup>2</sup>Deutsches Elektronen-Synchrotron DESY, Notkestr. 85, 22607 Hamburg, Germany. <sup>3</sup>SLAC National Accelerator Laboratory, Menlo Park, CA 94025, USA. <sup>4</sup>DLR (Deutsches Zentrum für Luft und Raumfahrt) Institute of Networked Energy Systems, Carl-von-Ossietzky-Str.15, 26129 Oldenburg, Germany. ✉email: stefan.funkner@kit.edu

With respect to MBI, the electron bunch might be regarded as a non-equilibrium thermodynamic system with a steady flow of energy exhibiting rich structural and dynamic self-organized patterns<sup>12</sup> similar to other non-equilibrium thermodynamic systems, such as the Rayleigh–Bérnard convection, Turing instability or the Belousov–Zhabotinsky reaction<sup>13</sup>. Here, a deep understanding of the physical laws determining the development of the electron bunch density bears the potential to further control or stabilize the occurrence of the CSR bursts, which then could provide a bright THz radiation source for user applications<sup>14</sup>. The details of the dynamics during the MBI are, however, still unclear and subject of intense research efforts<sup>15–30</sup>.

With respect to accelerator diagnostics, measuring the phase space distribution (PSD) of the electron bunch is key to a complete characterization of its physical state. While phase space dynamics can be simulated with great detail (for example by numerically solving the corresponding Vlasov–Fokker–Planck equation<sup>21,25</sup>), for non-destructive experiments with electron bunches the PSD remains an elusive quantity. Early ideas by Hancock et al.<sup>31</sup> for the reconstruction of the longitudinal PSD of proton bunches and other concepts for heavy ion colliders<sup>32</sup>, linear accelerators<sup>33,34</sup> as well as theoretical considerations<sup>35</sup>, did not mature into a diagnostic tool for electron storage rings. Here, challenges from the high revolution frequencies and fading out of information about substructures in the far-field have to be overcome. Hence, many interpretations of experimental results can only be taken as indirect conclusions about the state of the PSD of the electron bunches.

In this paper, we describe how this diagnostics gap can be closed using single-shot electro-optical (EO) sampling of the electron bunch near-field in combination with turn-by-turn measurements at MHz repetition rates using an ultra-fast line-array detection system<sup>36</sup>. The longitudinal PSD not only determines the emission spectrum of the bunch, but also provides insights in other fundamental properties such as bunch length, energy spread or, more sophisticated, relativistic intra-bunch interactions. Throughout the paper we restrict our attention to the longitudinal PSD. We therefore consider only the spatial coordinate in the direction of the bunch motion and approximate the bunch as one-dimensional line charge density.

## Results

**Reconstruction method.** The working principle of our setup is visualized in Fig. 1 (see<sup>39</sup> for a detailed description): to measure the charge density of a relativistic bunch we overlap broadband linearly polarized chirped laser pulses from a fiber laser with the Coulomb field of the electron bunch in a gallium phosphide EO crystal. The timing is adjusted by a phase-locked loop synchronizing the laser repetition rate to the revolution frequency of the storage ring. Due to the relativistic motion of the bunch, the Coulomb field of an individual relativistic electron is highly compressed perpendicular to its motion in a radial pancake-like structure. Consequently, the time-dependent Coulomb field of the electron bunch leaked into the EO crystal is proportional to the charge density profile. Due to the chirp in the linearly polarized laser beam, the charge density profile is imprinted on the laser pulse as a wavelength dependent change of the polarization.

In the next stage, this information is transformed into a wavelength dependent intensity profile by a polarizing cube beam splitter. In this process, the wavelength encodes the time-dependence. The profile is finally decoded by a grating and read out by an ultra-fast line array camera<sup>36</sup> in the spectral domain. By comparing the intensity profile of the laser pulse to a reference measurement, taken without the presence of electrons, we can directly deduce the longitudinal charge profile of the electron bunch<sup>39</sup>.

From the bunch profile measurements, we can reconstruct the PSD using the following approximation: during the time of half a synchrotron oscillation period (in our case  $\sim 61 \mu\text{s}$ ), we assume that the change of the microstructures is small. Then the resulting dynamics can be described by a well-known rotation of the PSD<sup>24</sup>, which is a result of the phase focusing of the electron bunch to the radio frequency system of the storage ring<sup>43</sup>. In other words, to pick a reasonable transformation, we approximate for a moment the dynamics of the PSD by a rigid rotation with a rotation period of  $\sim 122 \mu\text{s}$ .

In Fig. 2a, we show a typical configuration of the PSD taken from a simulation of the electron bunch dynamics based on the Vlasov-Fokker-Planck equation using Inovesa, a simulation program developed at the Karlsruhe Institute of Technology (KIT)<sup>25</sup>. With respect to phase space, an EO near-field measurement can be interpreted as a projection of the PSD onto the axis related to a generalized coordinate (in our case we measure the arrival time). During consecutive measurements, performed on a turn-by-turn basis by our setup, the PSD of the

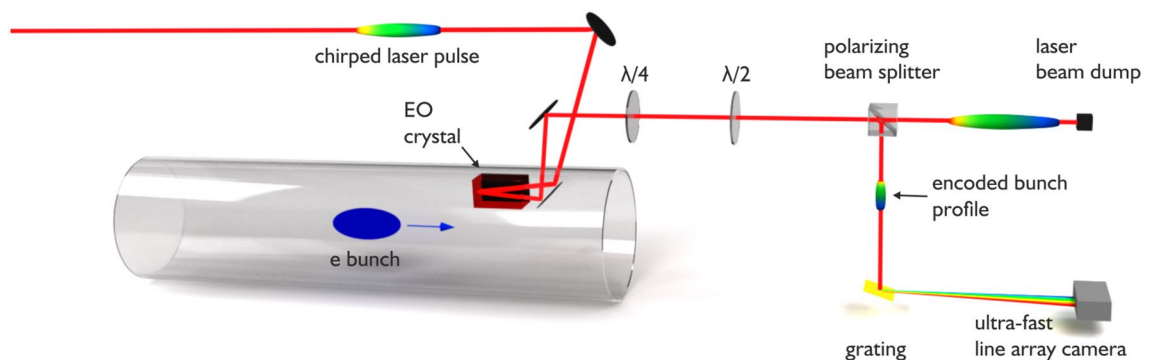


**Figure 1.** The setup to measure charge density profiles of electron bunches in a storage ring with single-shot electro-optical sampling of the near-field is shown (see<sup>37–39</sup>). The closed metallic beam pipe of the accelerator is here indicated as a transparent cylinder.

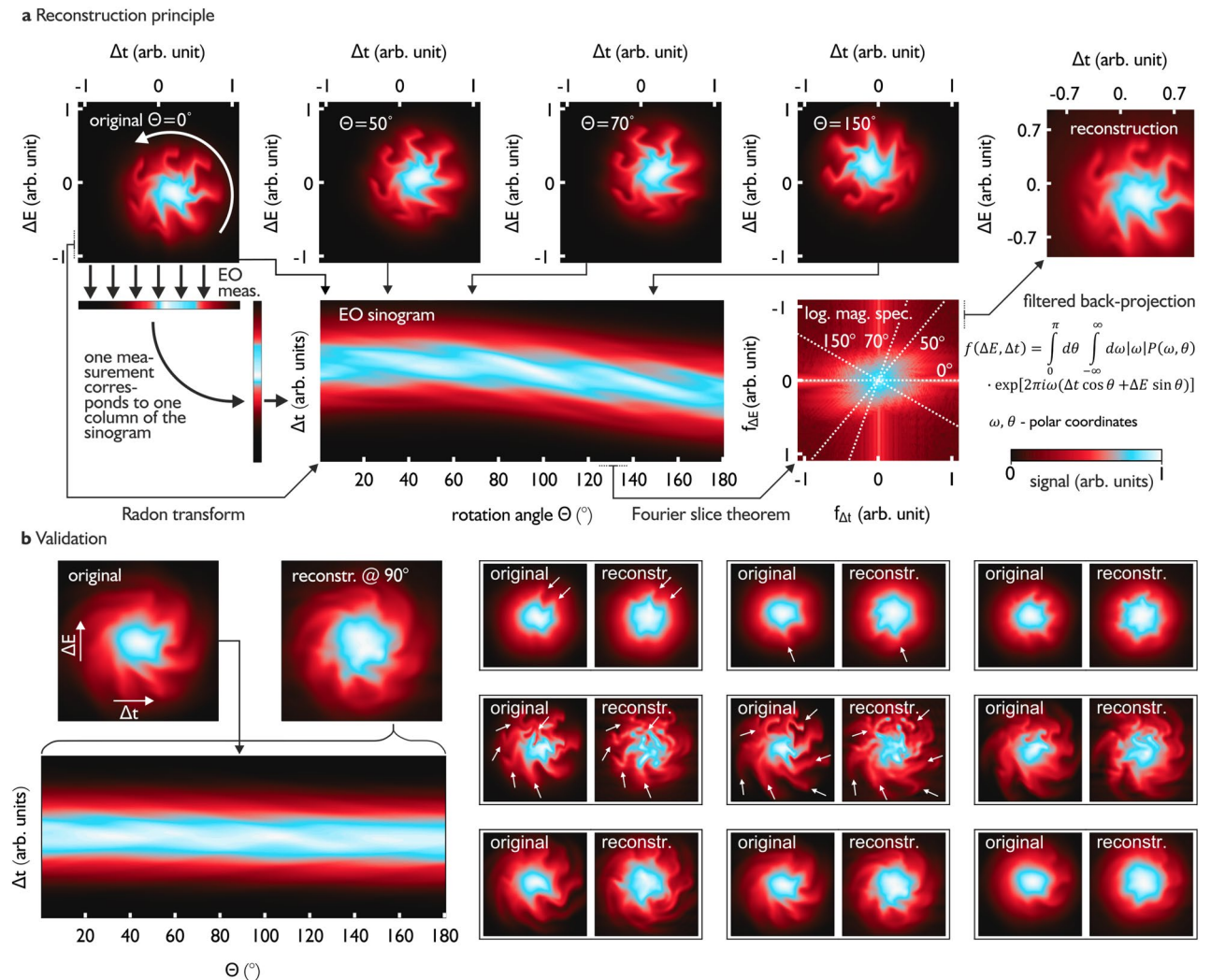


**Figure 2.** (a) Reconstruction principle of the PSD distribution with electro-optical sampling (illustrated by a simulated phase space configuration). Top: we assume a rigid rotation. Shown are the PSD configurations at different rotation angles and the final reconstruction. Bottom: the EO measurement (projection on the time axis) of the different PSD configurations can be interpreted as a Radon transform. Each PSD configuration is represented by a single column in the corresponding sinogram. The Radon transform is connected to the 2D Fourier transform of the original image via the Fourier slice theorem<sup>40</sup>. The original PSD can be reconstructed with a filtered back-projection. (b) Validation of the reconstruction algorithm with simulated data obtained from the Vlasov–Fokker–Planck solver Inovesa<sup>25</sup>. We used a standard ramp filter to avoid the blurring effect of the back-projection<sup>40</sup> in combination with a high frequency cut-off at a relative frequency of 0.1 to reduce the exaggeration of edges. Left side: comparison between the original and reconstructed PSD. The “original” PSD is evaluated at the  $90^\circ$  frame, while for the reconstruction the complete sinogram has to be taken into account. Right side: several comparisons during different times of a bursting cycle. Even in situations with prominent substructures, where bunch self-interaction is expected to be strong, the reconstruction shows a reasonable agreement with the original PSD, also in fine details.

electron bunch rotates, so that the experiment can be interpreted as a tomographic measurement of the electron bunch PSD. If we concatenate consecutive measurements taken during half a rotation period we obtain, in this interpretation, the Radon transform of the PSD resulting in the so-called sinogram (see Fig. 2a bottom). The sinogram can be related to the 2D Fourier transform of the original image (or PSD) via the Fourier slice theorem<sup>40,44</sup>. The reconstruction of the PSD is then performed with a filtered back-projection<sup>44,45</sup>, a well-known procedure widely used for example in medicine for computed tomography scans.

**Validation of the proposed method via simulations.** The approximation of the PSD dynamics as a rigid rotation is an idealization. In fact, static deformation<sup>46,47</sup> as well as the dynamic formation of substructures<sup>48</sup> is caused by nonlinearities in the potential. Hence, to validate our approach for the condition present during the experiments we use Inovesa simulations<sup>25</sup>, which solve the Vlasov-Fokker-Planck equation numerically and are not constrained by the assumption of a rigid rotation. Our group already demonstrated that the



software can precisely predict the bunch current depending bursting behavior of electron bunches over long time scales<sup>25</sup>.

The simulations provide a PSD during every time step, so that we can calculate the EO sinogram (which is a simple projection) and compare the corresponding reconstructed PSD to the original simulated PSD. In Fig. 2b, we show that even though the PSD dynamics can be complicated during the MBI due to collective effects of the microstructures, the filtered back-projection can not only reconstruct the PSD on a coarse grained level, but also resolve subtleties of the microstructures (we marked a few of them with white arrows). From this point of view, we interpret the proposed method as a powerful reconstruction algorithm - independent of previously made assumptions to find the right procedure.

**Experimental phase space tomography of electron bunches in a storage ring.** To demonstrate this principle experimentally, we measured profiles of a single electron bunch during the MBI at the Karlsruhe Research Accelerator (KARA). During the experiments, the bunch contained roughly  $2 \times 10^9$  electrons and was accelerated to a highly relativistic motion with a Lorentz factor  $\gamma \approx 2500$ . To induce the MBI, we compressed the longitudinal bunch size with the low- $\alpha_c$  mode of the storage ring to a few picoseconds. We then observed the development of the bunch profile at a repetition rate of 2.72 MHz corresponding to its revolution time in the storage ring.

In Fig. 3a, we show three different sections each consisting of 6000 successive profile measurements stacked from left to right. The sections are part of a larger data set with 500,000 turn-by-turn measurements. The representation of the sections in Fig. 3a is also referred to as “revolution plot”<sup>39</sup>. With respect to interpretations utilizing the Radon transformation, a sinogram is a short revolution plot, which comprises a  $180^\circ$  rotation of the phase space—the data content necessary to reconstruct a tomogram. In each displayed revolution plot, the

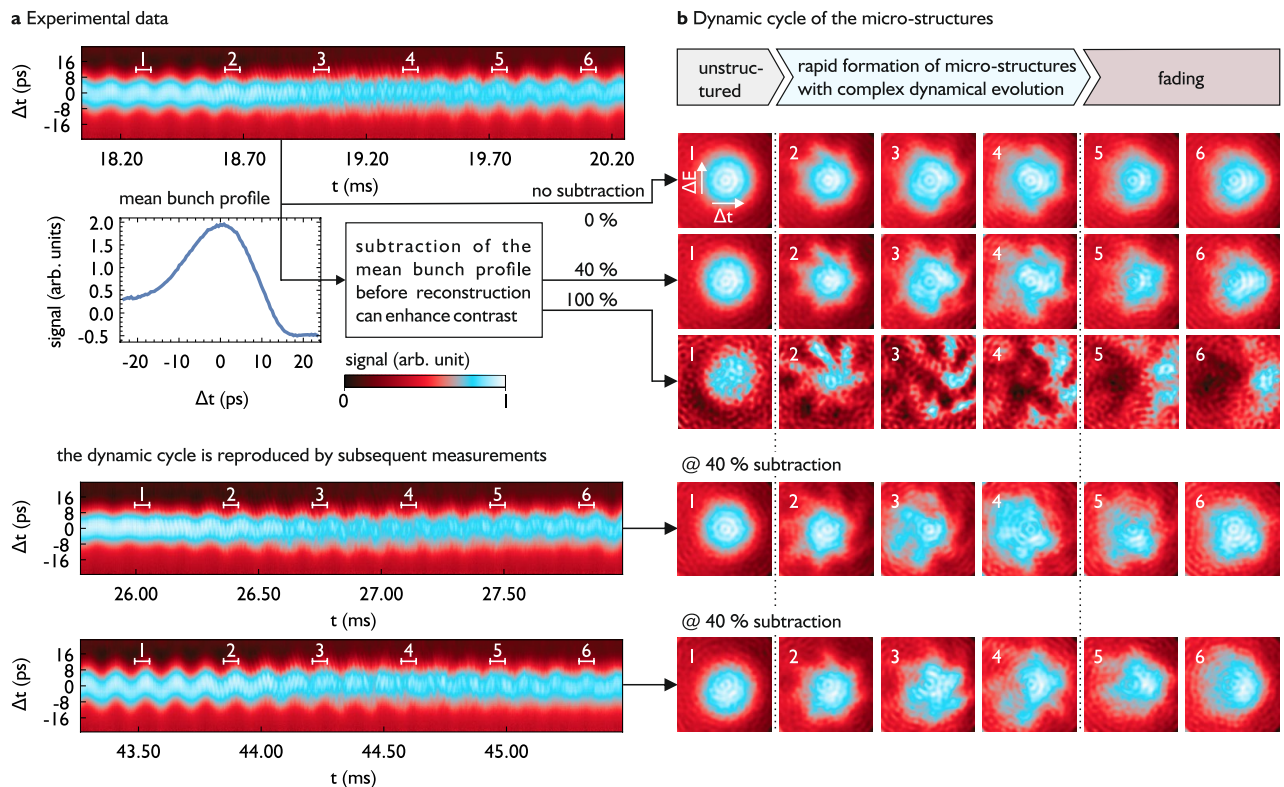


**Figure 3.** Experimental data: (a) Three revolution plots of 6000 consecutive measurements (corresponding to 18 synchrotron oscillations) of the electron bunch charge density taken from a longer data set with 500,000 measurements ( $\sim 0.18$  s). For each revolution plot, the measurements are concatenated from left to right. The value for  $\Delta t$  is determined by the pixel number of the line array, calibration measurements<sup>39</sup> and the mean bunch profile position. (b) Corresponding reconstructions of the PSD for different time intervals. The numbers refer to the time intervals marked in the revolution plots on the left side, respectively. Upper side: reconstructions for different subtraction percentages of the mean bunch profile are compared for the first revolution plot. The dynamic cycle of the microbunching instability is repeated over and over again, as it can be seen by comparing the rows of the reconstructed PSDs for the different revolution plots. In the supplement, we provide an animation of the PSD development, which is derived from the first revolution plot. To provide the optimal contrast, we normalized the data for every image independently. The color scale of the present and previous Fig. was calculated from a data set provided by P Kovacs<sup>41,42</sup>. An independent calculated gray scale image is provided by the supplementary Fig. S1.

noise-induced<sup>49</sup> coherent synchrotron oscillation appears as a clearly visible center of mass oscillation of the bunch profile.

We utilize this effect to determine the synchrotron oscillation period, which is needed to extract the sinograms for PSD reconstruction: if we consider a horizontal cross section in the revolution plots, the center position of the bunch profiles moves due to the longitudinal synchrotron oscillation. Hence, the frequency of the synchrotron oscillation can be conveniently determined from the data set using a Fourier transform. To provide a precise estimation, we used all bunch profiles of the data set and averaged the resulting spectrum along the horizontal cross sections. In the case shown here, the synchrotron oscillation frequency is estimated to be 8.28 kHz corresponding to 328 turns. Parallel measurements with beam position monitors estimate a value of 8.24 kHz, which is an insignificant difference with respect to the further discussions. Therefore, roughly 18 synchrotron oscillations are displayed for each revolution plot in Fig. 3a.

From the determination of the synchrotron oscillation frequency, we conclude that a PSD reconstruction can be performed from a sinogram consisting of about  $328/2 = 164$  consecutive measurements (the angle resolution is about  $1.1^\circ$ ), i.e. a sinogram corresponds to a revolution plot with 164 measurements (angular phase space projections). In order to guarantee a good resolution of the phase space reconstruction, the number of angular projections should be at least  $n_\theta = (\pi/2)n_R$ <sup>50</sup>, where  $n_R$  is the number of illuminated pixels. As it is explained in the methods section, we used 106–108 pixels of our line array camera for phase space reconstruction. Thus, the number of recommended angular projections is about 167–170, which is close to the 164 projections in our experiment, which emphasizes the need for turn-by-turn line array measurements at 2.72 MHz in relation to the number of used pixels.

In Fig. 3b, we show reconstructions of the PSD during different times. For the calculations we used a filtered back-projection with a ramp filter<sup>40</sup>. Compared to the simulations, we sampled every bunch profile (with 106–108 pixels) at a rate that is more than two times lower. Here, we doubled the high frequency cut-off for the filtered back-projection from 0.1 to 0.2 of the highest frequency to roughly compensate for the lower sampling rate. The time intervals used for every reconstruction are indicated in each revolution plot in Fig. 3a as white horizontal lines. Each of these short intervals on its own can be regarded as a sinogram of the PSD.

In general, the observed microstructuring of the bunch profile is small compared to the overall profile. For the top revolution plot in Fig. 3, we show how the contrast of the PSD reconstructions can be enhanced: we calculate the mean bunch profile for each revolution plot and subtract a scaled version from every bunch profile before applying the filtered back-projection. Such a procedure might introduce artifacts and should be handled carefully. A comparison for different scaling factors is visible at the top of Fig. 3b. We note that a 40% subtraction can improve the contrast significantly without introducing additional features (deduced from a careful comparison with the PSD at 0% subtraction) as it might be the case when subtracting 100% of the mean bunch profile. By comparing the measured PSDs in Fig. 3 with the simulated ones in Fig. 2 it can be seen that the MBI structures in the PSD visible in the simulations are qualitatively well represented in the measured data. A complete comparison between all discussed subtraction schemes and investigated microbunching cycles is displayed in the supplementary Fig. S2.

In the next step, we use the measured PSDs, to analyze the development and the structure of the electron bunch distribution in phase-space. We first analyze the PSD reconstruction from the revolution plot in Fig. 3a at the top: at the beginning of the measurement, substructures due to the MBI are not visible in the revolution plot at time interval 1. Hence, the PSD, shown in the first column of Fig. 3b, corresponds approximately to a 2D Gaussian-like distribution as expected. In the further development, diagonal stripes appear in the revolution plot. Here, the reconstruction of the PSD in Fig. 3b at column 2 shows a star-like structuring with a symmetry center roughly located at the center of mass position. Afterwards, the structure of the PSD during time intervals 3 and 4 undergoes a complex dynamic development and the stripe pattern becomes irregular. Finally, during the time intervals 5 and 6, the stripe pattern becomes less visible and the PSD images correspond to Gaussian distributions overlaid with weak substructures. This relaxation during which the substructures disappear takes rather long in comparison to the fast appearance of the substructures in the beginning. The overall process shown here retraces a typical excitation and relaxation cycle during the MBI<sup>53</sup>. This is underlined by the reproduced dynamics demonstrated by the reconstructions for the two other revolution plots in Fig. 3a.

While this shows how the overall dynamics can be easily analyzed with the reconstructed PSDs, it is also possible to extract information about the dynamical development of structural features of the PSD. As an illustrative application, we calculated all PSDs during one complete synchrotron oscillation period starting at 18.74 ms of the measured data set (around the second step of the dynamic cycle in the first revolution plot in Fig. 3), where a star-like shape with a 7-fold symmetry is observed. In the next step, we investigate the correlation of every image with the reference frame obtained from the first 164 revolutions using a simple Euclidean distance<sup>51,52</sup>. The result, shown in Fig. 4, features a well-defined oscillatory pattern. For the interpretation of the results it is important to note, that the reconstructed PSDs from time intervals up to half a synchrotron period after the reference frame are statistically dependent. This is due to the overlapping data used for the reconstructions (i.e. a sliding window is used for the turn-by-turn reconstructions). Therefore, the correlation should be investigated for more than half a synchrotron oscillation period, such as in Fig. 4, where the oscillatory pattern is recorded for a complete synchrotron oscillation period.

While a distinct reconstruction provides structural information, the correlation of the PSD over time adds dynamic information, which is different from a self-correlation of a single PSD measurement. Here, the clear occurrence of seven minima indicates that the star-like structures of the PSD plots (in Fig. 4) have a 7-fold symmetry and might rotate with a rigid  $360^\circ$  motion during one complete synchrotron oscillation period, similar to the model in<sup>54</sup>. This situation might change for other times, different dynamic regimes of the MBI and different experimental settings of the storage ring. Since we did not enhance the contrast of the PSD reconstruction by

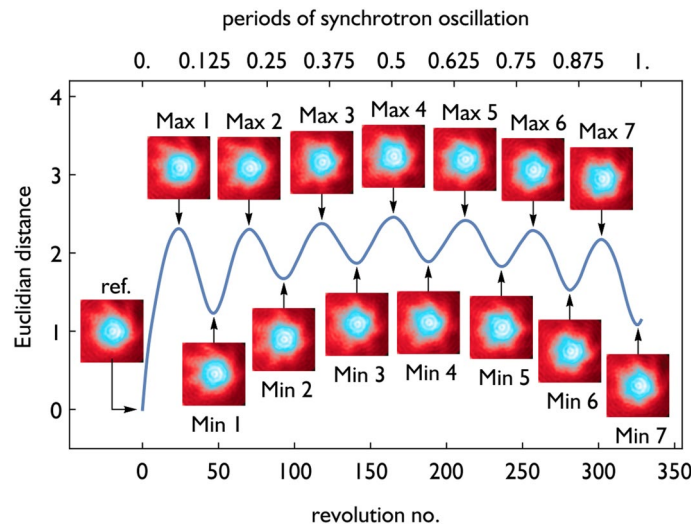


**Figure 4.** The Euclidian distance<sup>51,52</sup> between a reference PSD and each PSD from the subsequent data is shown (in blue). The PSD configurations at the minima and maxima as well as the reference PSD are displayed as insets. The Euclidian distance follows an oscillatory pattern as expected from a complete rigid rotation of a PSD structure with 7-fold symmetry.

mean bunch profile subtraction for this correlation study, this method demonstrates how situations with even challenging signal-to-noise ratios can be handled.

Finally, the Euclidean distance shows a slow but significant up and down bending, particularly visible at the progression of the minima positions. We attribute this effect to a mismatch between the rotation center and the center of gravity of the PSD (rather than an asymmetry of the PSD itself), which is consistent with the observation of the synchrotron oscillation in the revolution plots<sup>49</sup> (even when the substructures are faded out, see especially Fig. 3).

In summary, we demonstrated a robust method to reconstruct the longitudinal PSD from turn-by-turn measurements of the longitudinal bunch profile using a filtered back-projection. In doing so we close an important diagnostics gap for electron storage rings. Our approach is based on the approximation of the electron bunch dynamics by a rigid rotation of the PSD during half a synchrotron oscillation period. From comparison to simulations, we provide empirical evidence, that the filtered back-projection performs very well, even under conditions with strong intra-bunch interactions. Applying the PSD reconstruction to experimental data, we are able to observe a typical dynamic cycle in a reproducible manner.

For future research, it might be interesting to analyze the filtered back-projection performance with respect to the PSD dynamics governed by the Vlasov–Fokker–Planck equation more deeply. Moreover, considering that the filtered back-projection is originally not intended to be used for PSD tomography of electron bunches, it might be possible to construct a specialized algorithm deduced from the Vlasov–Fokker–Planck equation relaxing the rigid rotation assumption.

We investigated phase space reconstructions during the microbunching instability for specific machine settings of the KARA storage ring. We can assume that the electron-beam parameters can be slightly different, and the method should still be applicable. However, electron bunch dynamics depend on those parameters leading to different regimes<sup>30</sup> and parameter spaces of stability, slow oscillations or more rapid variations. Future investigations could help to explore the parameter space applicable to our method. If dynamics are rapidly changing during one orbit, additional measurement systems distributed along the storage ring could provide sufficient samples to reconstruct the PSD also in those regimes. An improvement of the background suppression resulting from an advanced analysis of various background sources might further improve the contrast and accuracy of the reconstructed PSDs.

Finally, our approach offers a glimpse into the physics of equilibrium/non-equilibrium ultrarelativistic systems. It therefore supports the development of advanced accelerator concepts with low energy footprints, where coherent emission from compressed, high-density electron beams plays an important role<sup>55</sup>.

## Methods

**Experimental parameters and setup.** The measurements were enabled through an synchronized interplay between three instruments: an accelerator providing strongly self-interacting relativistic electron bunches, a single-shot EO sampling experiment using a synchronized laser system and a fast line array camera system measuring at MHz repetition rates.

The experiments were conducted at the Karlsruhe Research Accelerator (KARA), which was operated in a dedicated short bunch mode<sup>56,57</sup> to compress the bunch length to a few picoseconds (< 17.8ps). The machine parameter settings, which were similar to those in reference<sup>30</sup>, are displayed in Table 1a. During the measurements, the beam energy was set to 1.3 GeV and a radio frequency voltage of 799 kV was applied. The data of

Parameter	Value	Parameter	Value
(a) Particle accelerator settings and parameters during the experiment		(b) Parameter settings used for the Inovesa simulations of the PSD dynamics and derived parameters	
Beam energy	1.29 GeV	Beam energy	1.285 GeV
Calculated relative energy spread	$4.7 \times 10^{-4}$	Natural relative energy spread	$4.7 \cdot 10^{-4}$
Bunch current	0.85 mA	Bunch current	0.85 mA
Radio frequency voltage	799 kV	Radio frequency voltage	799.257 kV
Radio frequency	499.73 MHz	Radio frequency* $f_{RF}$	499.72928 MHz
Synchrotron frequency	8.28 kHz	Synchrotron frequency	8.256 kHz
Revolution frequency	2.7159 MHz	Revolution frequency $f_r$	2.71592 MHz
Vacuum chamber height	32 mm	Vacuum chamber height	32 mm
Calc. momentum compaction factor	$5 \times 10^{-4}$	Momentum compaction factor	$5 \cdot 10^{-4}$
Circumference	110.4 m	Circumference	not a model parameter
Harmonic number $h$	184	Harmonic number $h$	184
Damping time	not measured	Damping time	10.4 ms

**Table 1.** Parameters. \*Derived parameters from the settings corresponding to the accelerator experimental conditions:  $f_{RF} = h \cdot f_r$

Fig. 3 was taken at a bunch current of 0.85 mA in single bunch operation mode at the so-called sawtooth bursting regime (see<sup>30</sup>).

For the EO measurement, we used chirped laser pulses from a custom-built regenerative amplifier<sup>38</sup> with a central wavelength of 1050 nm, an optical power of a few mW and a spectral width of about 80 nm. The ytterbium-doped fiber oscillator of the laser system operates at 62.5 MHz and is actively synchronized to the 8th subharmonic of the 500 MHz master oscillator. A pulse-picker is then used to reduce the repetition rate of the laser system (see also<sup>39</sup> for further details).

Afterwards, the spectrum of the laser pulses was resolved by a grating and measured with the KIT-developed ultra-fast spectrometer KALYPSO<sup>36</sup> (KARlsruhe Linear arraY detector for MHz-rePetition rate SpectrOscopy) using a 256-pixel back-illuminated silicon line array. The repetition rate of the line array readout was 2.72 MHz, so that that the electron bunch profile was detected on a turn-by-turn basis.

**Details of the post-measurement data processing and the back-projection parameters.** To calculate the bunch profile, we first determine the background signal of the line array by blocking the laser beam. In the next step, we record the signal of the laser pulses propagation through the EO (GaP) crystal without the overlap with the electron bunch. To do so, the phase of the laser synchronization system is changed, so that the laser pulse arrives before the electron bunch at the EO crystal. We subtract the background signal from the measurements with and without overlap and obtain the modulated and unmodulated signal. The result is shown in Fig. 5a.

The gray and black curves display the unmodulated and modulated signals, respectively. The edges of the line array are not illuminated by the laser pulses. The data acquisition of the 256-pixel line array is realized by two Gotthard chips reading out 128 pixel arrays each. The negative values at the intervals pictured in Fig. 5a and the kink between the pixel 128 and pixel 129 indicate that the measured intensities are reduced by a constant offset different for each Gotthard chip. For further calculations, we determined these offsets by averaging the intensity for all measurements in the regions indicated by the intervals in Fig. 5a. Afterwards, the offsets were removed from every data set. Figure 5a displays in red and blue the corrected values for the modulated and unmodulated signals. Especially the kink is reduced significantly for these data sets. With the corrected data, we calculated the bunch profiles according to<sup>39</sup> by dividing the modulated by the unmodulated signal and subtracting 1 from the result.

In the next step we determined which pixel should be considered for further analysis. Clearly such a decision depends on the signal-to-noise ratio for the calculated charge density of the bunch profiles. Here we used the following criterion: we consider all pixels for which half of the maximum signal modulation can be distinguished from a background signal with an accuracy of 90 %. We assume that the maximum signal is about 0.2 (determined from average bunch profiles). As described in<sup>39</sup>, if  $\sigma_{\bar{\rho},i}$  is the standard deviation for a hypothetical repeated, single-shot measurement for pixel  $i$ , then we consider all pixels for which the selection criterion

$$0.1 - 1.645\sigma_{\bar{\rho},i} > 0 \quad (1)$$

is fulfilled. Figure 5b displays the dependence of  $\sigma_{\bar{\rho}}$  on the pixel number. From this procedure the pixels numbers between 48 and 201 are selected. While Eq. (1) provides an objective and reproducible measure, which data should be considered for further evaluation, the reconstruction of the PSD needs further refinement.

For the filtered back-projection it is assumed that the PSD rotates around a center point, which is located in the middle of the sinogram. Thus, we have to determine at which pixel the center point of rotation is located and then further cut the considered data range symmetrically around this center point. In order to calculate this



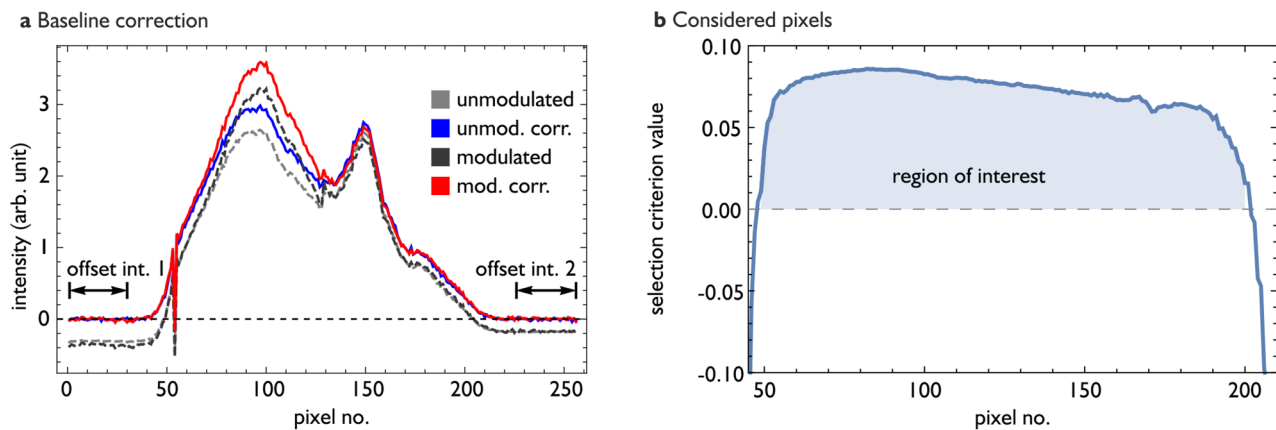


**Figure 5.** (a) Removal of the Gotthard chip dependent offset from the measured data. (b) Definition of the region of interest. Details see main text.

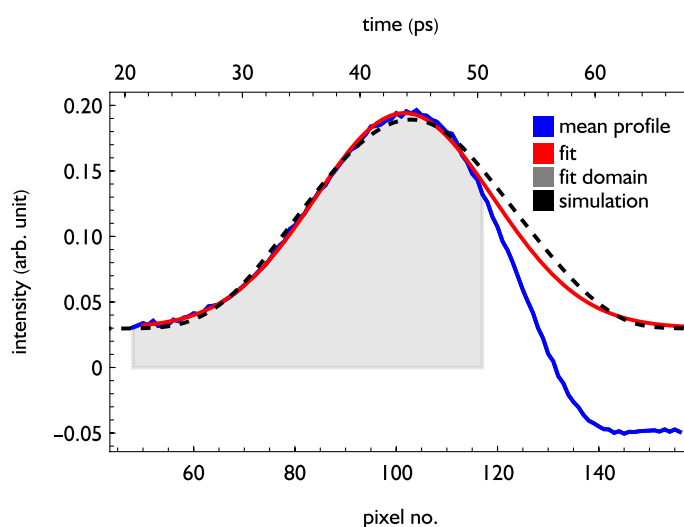


**Figure 6.** Determination of the rotation center shown for the case of first revolution plot in Fig. 3. Pixel no. 102 is located closest to the center point. The black dashed line displays the mean bunch profile from our simulations. The time axis shown for the experimental data is calculated from calibration measurements<sup>39</sup>.

center point, we average all bunch profiles in a section for which the reconstruction is considered (see Fig. 6). We then fit a normal distribution to the bunch profile considering only pixels from 48 to 114, because the right side of the profile (later in time) is overlapping with the wake field of the electron bunch<sup>58</sup>, which results in a distortion of the line shape.

Due to our measurement principle, field components from the electron bunch that do not co-propagate with the laser beam are suppressed in the measured polarization signal. This filter effect will be stronger for signals from (microbunching-)substructures, because the interaction length decreases for shorter non-collinear signals.

Figure 6 visualizes the calculation of the center point for the first section in Fig. 3a. The mean of the normal distribution is closest to pixel 102. For the other sections in Fig. 3b, we obtain similar fits, and with pixel 102 and pixel 101 we also find similar corresponding means. Finally, we chose the largest interval for which the center rotation point is in the middle and which is part of the interval from pixel 48 and 201. Thus, for the first two revolution plots, we used the pixels between pixel 48 and 156 and for the last revolution plot we used the pixels between 48 and 154. In general, these small differences have no influence on the data interpretation at the current signal-to-noise ratio, i.e. it would be also possible to use the same interval for all reconstructions.

For further comparison, we displayed in Fig. 6 the mean bunch profile from our simulated data (dashed) showing a good agreement with the normal distribution (red), which we used for the fit. It should be noted that due to the averaging process fine details are smoothed out. From the fitted normal distribution in Fig. 6 we estimate a bunch length (FWHM) of  $17.8 \pm 0.15$  ps including the broadening by the synchrotron oscillation. Here, fits to every turn-by-turn measurement result, at similar experimental conditions, in comparable values<sup>59</sup>.



**Settings of the Inovesa simulations.** To validate the reconstruction empirically under the conditions present during the experiment, we simulate the PSD dynamics by numerically solving the Vlasov-Fokker-Planck equation using the Inovesa software program.

The PSDs shown in Fig. 2 were simulated using Inovesa v1.1.0 (10.5281/zenodo.3466767). This version implements the phase noise of the radio frequency cavities exciting the synchrotron oscillation, which is typically not part of simulations<sup>60</sup>. The resulting potential is modified by the wake potential due to self-interaction with the CSR of the bunch and calculated according to the parallel plates shielding model<sup>61</sup>. The simulations were carried out with a bunch current of 0.85 mA—closely to the experimental conditions. With these settings, the simulations cover, very similar to the experimental situation, the sawtooth bursting regime. We used 164 profile measurements for reconstructions of the PSDs. Every profile was sampled with 256 pixels. The list of used parameters is displayed in Table 1b.

## Data availability

The datasets used and/or analyzed during the current study are available from the corresponding author on reasonable request.

Received: 19 October 2022; Accepted: 7 March 2023

Published online: 21 March 2023

## References

1. Arnold, A. *et al.* Entropies and equilibria of many-particle systems: an essay on recent research. *Mon. Math.* **142**, 35–43. <https://doi.org/10.1007/s00605-004-0239-2> (2004).
2. Alder, B. J. & Wainwright, T. E. Studies in molecular dynamics. I. General method. *J. Chem. Phys.* **31**, 459–466. <https://doi.org/10.1063/1.1730376> (1959).
3. Helbing, D. Traffic and related self-driven many-particle systems. *Rev. Mod. Phys.* **73**, 1067–1141. <https://doi.org/10.1103/RevModPhys.73.1067> (2001).
4. Negele, J. W. & Orland, H. *Quantum Many-Particle Systems* 1st edn. (CRC Press, Boca Raton, 2018).
5. Schwinger, J. On radiation by electrons in a betatron: Transcription of a paper by J. Schwinger, 1945. Tech. Rep., Lawrence Berkeley National Laboratory (LBNL), Berkeley (1996). <https://doi.org/10.2172/1195620>.
6. Schiff, L. I. Production of particle energies beyond 200 Mev. *Rev. Sci. Instrum.* **17**, 6–14. <https://doi.org/10.1063/1.1770395> (1946).
7. Billinghurst, B. E. *et al.* Longitudinal bunch dynamics study with coherent synchrotron radiation. *Phys. Rev. Accel. Beams* **19**, 20704. <https://doi.org/10.1103/PhysRevAccelBeams.19.20704> (2016).
8. Tammaro, S. *et al.* High density terahertz frequency comb produced by coherent synchrotron radiation. *Nat. Commun.* **6**, 7733. <https://doi.org/10.1038/ncomms8733> (2015).
9. Venturini, M. & Warnock, R. Bursts of coherent synchrotron radiation in electron storage rings: A dynamical model. *Phys. Rev. Lett.* **89**, 224802. <https://doi.org/10.1103/PhysRevLett.89.224802> (2002).
10. Abo-Bakr, M., Feikes, J., Holladack, K., Wüstefeld, G. & Hübers, H.-W. Steady-state far-infrared coherent synchrotron radiation detected at BESSY II. *Phys. Rev. Lett.* **88**, 254801. <https://doi.org/10.1103/PhysRevLett.88.254801> (2002).
11. Stupakov, G. & Heifets, S. Beam instability and microbunching due to coherent synchrotron radiation. *Phys. Rev. Spec. Top. Accel. Beams* **5**, 054402. <https://doi.org/10.1103/PhysRevSTAB.5.054402> (2002).
12. Bielawski, S. *et al.* From self-organization in relativistic electron bunches to coherent synchrotron light: Observation using a photonic time-stretch digitizer. *Sci. Rep.* **9**, 10391. <https://doi.org/10.1038/s41598-019-45024-2> (2019).
13. Cross, M. C. & Hohenberg, P. C. Pattern formation outside of equilibrium. *Rev. Mod. Phys.* **65**, 851–1112. <https://doi.org/10.1103/RevModPhys.65.851> (1993).
14. Evain, C. *et al.* Stable coherent terahertz synchrotron radiation from controlled relativistic electron bunches. *Nat. Phys.* <https://doi.org/10.1038/s41567-019-0488-6> (2019).
15. Roussel, E. *et al.* Observing microscopic structures of a relativistic object using a time-stretch strategy. *Sci. Rep.* **5**, 10330. <https://doi.org/10.1038/srep10330> (2015).
16. Wüstefeld, G. *et al.* Coherent THz measurements at the metrology light source. In International Particle Accelerator Conference, Kyoto, Japan. Place of publication: Joint Accelerator Conferences Website (JACoW). Paper WEPEA015 (2010, June) (2010).
17. Abo-Bakr, M., Feikes, J., Holladack, K., Kuske, P. & Wüstefeld, G. Coherent emission of synchrotron radiation and longitudinal instabilities. In Proceedings of the 2003 Bipolar/BiCMOS Circuits and Technology Meeting (IEEE Cat. No.03CH37440), vol. 5, 3023–3025. <https://doi.org/10.1109/PAC.2003.1289801> (IEEE, 2003).
18. Sannibale, F. *et al.* A model describing stable coherent synchrotron radiation in storage rings. *Phys. Rev. Lett.* **93**, 094801. <https://doi.org/10.1103/PhysRevLett.93.094801> (2004).
19. Byrd, J. M. *et al.* Laser seeding of the storage-ring microbunching instability for high-power coherent terahertz radiation. *Phys. Rev. Lett.* **97**, 074802. <https://doi.org/10.1103/PhysRevLett.97.074802> (2006).
20. Shields, W. *et al.* Microbunch instability observations from a THz detector at diamond light source. *J. Phys.: Conf. Ser.* **357**, 012037. <https://doi.org/10.1088/1742-6596/357/1/012037> (2012).
21. Warnock, R. L. & Ellison, J. A. A general method for propagation of the phase space distribution, with application to the sawtooth instability. In Proceedings of 2nd ICFA Advanced Workshop on The Physics of High Brightness Beams (University of California, LA, 1999), 322–348 (2000).
22. Bane, K. L. F., Cai, Y. & Stupakov, G. Threshold studies of the microwave instability in electron storage rings. *Phys. Rev. Spec. Top. Accel. Beams* **13**, 104402. <https://doi.org/10.1103/PhysRevSTAB.13.104402> (2010).
23. Evain, C. *et al.* Stable coherent terahertz synchrotron radiation from controlled relativistic electron bunches. *Nat. Phys.* **15**, 635–639. <https://doi.org/10.1038/s41567-019-0488-6> (2019).
24. Evain, C. *et al.* Spatio-temporal dynamics of relativistic electron bunches during the micro-bunching instability in storage rings. *EPL (Europhys. Lett.)* **98**, 40006. <https://doi.org/10.1209/0295-5075/98/40006> (2012).
25. Schönfeldt, P., Brosi, M., Schwarz, M., Steinmann, J. L. & Müller, A.-S. Parallelized Vlasov-Fokker-Planck solver for desktop personal computers. *Phys. Rev. Accel. Beams* **20**, 30704. <https://doi.org/10.1103/PhysRevAccelBeams.20.30704> (2017).
26. Brosi, M. *et al.* Systematic studies of the microbunching instability at very low bunch charges. *Phys. Rev. Accel. Beams* **22**, 020701. <https://doi.org/10.1103/PhysRevAccelBeams.22.020701> (2019).
27. Carr, G. L., Kramer, S. L., Murphy, J. B., Lobo, R. & Tanner, D. B. Observation of coherent synchrotron radiation from the NSLS VUV ring. *Nucl. Instrum. Methods Phys. Res. Sect. A* **463**, 387–392. [https://doi.org/10.1016/S0168-9002\(01\)00521-6](https://doi.org/10.1016/S0168-9002(01)00521-6) (2001).
28. Byrd, J. M. *et al.* Observation of broadband self-amplified spontaneous coherent terahertz synchrotron radiation in a storage ring. *Phys. Rev. Lett.* **89**, 224801. <https://doi.org/10.1103/PhysRevLett.89.224801> (2002).

29. Karantzoulis, E., Penco, G., Perucchi, A. & Lupi, S. Characterization of coherent THz radiation bursting regime at Elettra. *Infrared Phys. Technol.* **53**, 300–303. <https://doi.org/10.1016/j.infrared.2010.04.006> (2010).
30. Steinmann, J. L. *et al.* Continuous bunch-by-bunch spectroscopic investigation of the microbunching instability. *Phys. Rev. Accel. Beams* **21**, 110705. <https://doi.org/10.1103/PhysRevAccelBeams.21.110705> (2018).
31. Hancock, S., Lindroos, M. & Koscielniak, S. Longitudinal phase space tomography with space charge. *Phys. Rev. Spec. Top. Accel. Beams* **3**, 124202. <https://doi.org/10.1103/PhysRevSTAB.3.124202> (2000).
32. Montag, C., D’Imperio, N., Kewisch, J. & Lee, R. Tomographic phase space reconstruction during rebucketing in the relativistic heavy ion collider. *Phys. Rev. Spec. Top. Accel. Beams* **5**, 082801. <https://doi.org/10.1103/PhysRevSTAB.5.082801> (2002).
33. Yakimenko, V., Babzien, M., Ben-Zvi, I., Malone, R. & Wang, X.-J. Electron beam phase-space measurement using a high-precision tomography technique. *Phys. Rev. Spec. Top. Accel. Beams* **6**, 122801. <https://doi.org/10.1103/PhysRevSTAB.6.122801> (2003).
34. Hock, K. & Wolski, A. Tomographic reconstruction of the full 4D transverse phase space. *Nucl. Instrum. Methods Phys. Res. Sect. A* **726**, 8–16. <https://doi.org/10.1016/j.nima.2013.05.004> (2013).
35. Michelotti, L. Integral for longitudinal phase space tomography on equilibrium distributions. *Phys. Rev. Spec. Top. Accel. Beams* **6**, 024001. <https://doi.org/10.1103/PhysRevSTAB.6.024001> (2003).
36. Rota, L. *et al.* KALYPSO: Linear array detector for high-repetition rate and real-time beam diagnostics. *Nucl. Instrum. Methods Phys. Res. Sect. A* **936**, 10–13. <https://doi.org/10.1016/j.nima.2018.10.093> (2019).
37. Casalbuoni, S. *et al.* Numerical studies on the electro-optic detection of femtosecond electron bunches. *Phys. Rev. Spec. Top. Accel. Beams* **11**, 72802. <https://doi.org/10.1103/PhysRevSTAB.11.072802> (2008).
38. Müller, F. *et al.* Electro-optical measurement of sub-ps structures in low charge electron bunches. *Phys. Rev. Spec. Top. Accel. Beams* **15**, 070701. <https://doi.org/10.1103/PhysRevSTAB.15.070701> (2012).
39. Funkner, S. *et al.* High throughput data streaming of individual longitudinal electron bunch profiles. *Phys. Rev. Accel. Beams* **22**, 022801. <https://doi.org/10.1103/PhysRevAccelBeams.22.022801> (2019).
40. Buzug, T. M. *Computed Tomography* (Springer, 2008).
41. Kovsi, P. ColorCET-Perceptually Uniform Colour Maps. <https://peterkovsi.com/projects/colourmaps/>.
42. Kovsi, P. Good colour maps: How to design them (2015).
43. Wille, K. *The Physics of Particle Accelerators* (Clarendon Press, 2001).
44. Jähne, B. *Digitale Bildverarbeitung* 5th edn. (Springer, Berlin, 2005).
45. Wolfram Research. “InverseRadon”. <https://reference.wolfram.com/language/ref/InverseRadon.html> (2014).
46. Haissinski, J. Exact longitudinal equilibrium distribution of stored electrons in the presence of self-fields. *Il Nuovo Cimento B* **18**, 72–82 (1973).
47. Ng, K. Y. *Physics of Intensity Dependent Beam Instabilities* (World Scientific Publishing, Singapore, 2006).
48. Krinsky, S. & Wang, J. M. Longitudinal instabilities of bunched beams subject to a nonharmonic RF potential. *Part. Accel.* **17**, 109–139 (1985).
49. Ormond, K. W. & Rogers, J. T. Synchrotron oscillation driven by RF phase noise. In Proceedings of the 1997 Particle Accelerator Conference (Cat. No.97CH36167), vol. 2, 1822–1824. <https://doi.org/10.1109/PAC.1997.751029> (IEEE, 1997).
50. Somogyi, A. *et al.* Optical design and multi-length-scale scanning spectro-microscopy possibilities at the Nanoscopium beamline of Synchrotron Soleil. *J. Synchrotron Radiat.* **22**, 1118–1129. <https://doi.org/10.1107/S1600577515009364> (2015).
51. Nakhmani, A. & Tannenbaum, A. A new distance measure based on generalized Image Normalized Cross-Correlation for robust video tracking and image recognition. *Pattern Recogn. Lett.* **34**, 315–321. <https://doi.org/10.1016/j.patrec.2012.10.025> (2013).
52. Wang, Liwei, Zhang, Yan & Feng, Jufu. On the Euclidean distance of images. *IEEE Trans. Pattern Anal. Mach. Intell.* **27**, 1334–1339. <https://doi.org/10.1109/TPAMI.2005.165> (2005).
53. Kehrer, B. *et al.* Synchronous detection of longitudinal and transverse bunch signals at a storage ring. *Phys. Rev. Accel. Beams* **21**, 102803. <https://doi.org/10.1103/PhysRevAccelBeams.21.102803> (2018).
54. Roussel, E., Evain, C., Szwaj, C. & Bielański, S. Microbunching instability in storage rings: Link between phase-space structure and terahertz coherent synchrotron radiation radio-frequency spectra. *Phys. Rev. Spec. Top. Accel. Beams* **17**, 10701. <https://doi.org/10.1103/PhysRevSTAB.17.10701> (2014).
55. Seletskiy, S., Podobedov, B., Shen, Y. & Yang, X. Seeding, controlling, and benefiting from the microbunching instability. *Phys. Rev. Lett.* **111**, 34803. <https://doi.org/10.1103/PhysRevLett.111.034803> (2013).
56. Müller, A.-S. *et al.* Far infrared coherent synchrotron edge radiation at ANKA. In Proceedings of the 2005 Particle Accelerator Conference, 2518–2520. <https://doi.org/10.1109/PAC.2005.1591164> (IEEE, Knoxville, 2005).
57. Blomley, E. Investigation and Control of Beam Instabilities at the Karlsruhe Research Accelerator using a 3-D Digital Bunch-by-Bunch Feedback System. Ph.D. Thesis, Karlsruhe Institut für Technologie (KIT). <https://doi.org/10.5445/IR/1000137621> (2021).
58. Schönfeldt, P. *et al.* Towards near-field electro-optical bunch profile monitoring in a multi-bunch environment. In Proceedings of the 8th International Particle Accelerator Conference, Copenhagen, Denmark, 227–230. <https://doi.org/10.18429/JACoW-IPAC2017-MOPAB055> (JACoW, 2017).
59. Hiller, N. Electro-Optical Bunch Length Measurements at the ANKA Storage Ring. Ph.D. Thesis, Karlsruhe Institute of Technology (KIT) (2013).
60. Schönfeldt, P., Boltz, T., Mochihashi, A., Steinmann, J. L. & Müller, A.-S. Elaborated modeling of synchrotron motion in Vlasov-Fokker-Planck solvers. *J. Phys.: Conf. Ser.* **1067**, 062025. <https://doi.org/10.1088/1742-6596/1067/6/062025> (2018).
61. Murphy, J. B., Krinsky, S. & Gluckstern, R. L. Longitudinal Wakefield for an electron moving on a circular orbit. *Part. Accel.* **57**, 9–64 (1997).

## Acknowledgements

S.F. and B.K. were supported by BMBF contract No. 05K16VKA. E.B. and G.N. acknowledge support by the Helmholtz President’s strategic fund IVF “Plasma accelerators”. The authors thank N. Hiller, B. Härer, T. Boltz, M. Brosi, F. Donoso and P. Schreiber for fruitful discussions. The authors acknowledge support by the KIT-Publication Fund of the Karlsruhe Institute of Technology. We further thank J. Schmid and O. Speck for their technical support.

## Author contributions

The main projection management was conducted by A.S.M., M.W. and E.B.. S.F. analyzed the experimental and simulated data sets, implemented the filtered back-projection, prepared the figures and tables and wrote the first draft of the paper. G.N., M.J.N., E.B., B.K., J.L.S., P.S. and A.S.M. provided major revisions of the manuscript. G.N., S.F., M.J.N. enhanced and operated the EOSD experiment. G.N., S.F., B.S. prepared and aligned the laser system. L.R. and M.C. enabled measurements with their ultra-fast camera system KALYPSO. P.S. provided the simulated data and developed the corresponding Vlasov-Fokker-Planck solver “Inovesa”. M.S. operated the storage ring with the low-alpha optics. All authors reviewed the manuscript.

## Funding

Open Access funding enabled and organized by Projekt DEAL.

## Competing interests

The authors declare no competing interests.

## Additional information

**Supplementary Information** The online version contains supplementary material available at <https://doi.org/10.1038/s41598-023-31196-5>.

**Correspondence** and requests for materials should be addressed to S.F.

**Reprints and permissions information** is available at [www.nature.com/reprints](http://www.nature.com/reprints).

**Publisher's note** Springer Nature remains neutral with regard to jurisdictional claims in published maps and institutional affiliations.



**Open Access** This article is licensed under a Creative Commons Attribution 4.0 International License, which permits use, sharing, adaptation, distribution and reproduction in any medium or format, as long as you give appropriate credit to the original author(s) and the source, provide a link to the Creative Commons licence, and indicate if changes were made. The images or other third party material in this article are included in the article's Creative Commons licence, unless indicated otherwise in a credit line to the material. If material is not included in the article's Creative Commons licence and your intended use is not permitted by statutory regulation or exceeds the permitted use, you will need to obtain permission directly from the copyright holder. To view a copy of this licence, visit <http://creativecommons.org/licenses/by/4.0/>.

© The Author(s) 2023